

ARTICLE OPEN



ROR activation by Nobiletin enhances antitumor efficacy via suppression of I κ B/NF- κ B signaling in triple-negative breast cancer

Eunju Kim¹, Yoon-Jin Kim¹, Zhiwei Ji², Jin Muk Kang³, Marvin Wirianto¹, Keshav Raj Paudel¹, Joshua A. Smith^{4,5}, Kaori Ono¹, Jin-Ah Kim⁶, Kristin Eckel-Mahan⁷, Xiaobo Zhou², Hyun Kyoung Lee^{4,5}, Ji Young Yoo³, Seung-Hee Yoo¹✉ and Zheng Chen¹✉

© The Author(s) 2022, corrected publication 2022

Triple-negative breast cancer (TNBC) is a heterogeneous disease characterized by poor response to standard therapies and therefore unfavorable clinical outcomes. Better understanding of TNBC and new therapeutic strategies are urgently needed. ROR nuclear receptors are multifunctional transcription factors with important roles in circadian pathways and other processes including immunity and tumorigenesis. Nobiletin (NOB) is a natural compound known to display anticancer effects, and our previous studies showed that NOB activates RORs to enhance circadian rhythms and promote physiological fitness in mice. Here, we identified several TNBC cell lines being sensitive to NOB, by itself or in combination. Cell and xenograft experiments showed that NOB significantly inhibited TNBC cell proliferation and motility in vitro and in vivo. ROR loss- and gain-of-function studies showed concordant effects of the NOB–ROR axis on MDA-MB-231 cell growth. Mechanistically, we found that NOB activates ROR binding to the ROR response elements (RRE) of the I κ B α promoter, and NOB strongly inhibited p65 nuclear translocation. Consistent with transcriptomic analysis indicating cancer and NF- κ B signaling as major pathways altered by NOB, p65-inducible expression abolished NOB effects, illustrating a requisite role of NF- κ B suppression mediating the anti-TNBC effect of NOB. Finally, in vivo mouse xenograft studies showed that NOB enhanced the antitumor efficacy in mammary fat pad implanted TNBC, as a single agent or in combination with the chemotherapy agent Docetaxel. Together, our study highlights an anti-TNBC mechanism of ROR-NOB via suppression of NF- κ B signaling, suggesting novel preventive and chemotherapeutic strategies against this devastating disease.

Cell Death and Disease (2022)13:374; <https://doi.org/10.1038/s41419-022-04826-5>

INTRODUCTION

Triple-negative breast cancer (TNBC) is characterized by the lack of expression of estrogen receptor (ER), progesterone receptor (PR), and epidermal growth factor receptor 2 (HER2) [1]. It is a heterogeneous disease that can be subdivided to several subtypes based on histological and molecular features [2]. Compared with other breast cancers, it is resistant to commonly used hormone and targeted therapies, and patients often suffer aggressive tumor progression and less favorable outcomes as a result [1, 3]. Chemotherapies for TNBC, including taxanes and anthracyclines, are typically administered in a sequential single-agent regimen, and combination therapy remains a challenge mainly due to concerns of increased toxicity [1, 4]. Despite being the standard treatment, chemotherapies produce favorable response only in a subset of TNBC patients. Therefore, there is an urgent need for improved therapeutic regimens and

mechanistic understanding of TNBC responsiveness to specific agents [3, 5].

Citrus flavonoids, with varying degrees of methoxylation and glycosylation, display diverse beneficial effects in physiology and disease. In polymethoxylated flavonoids (PMFs) including Nobiletin (NOB) and its close analog Tangeretin, the methoxyl groups, in place of hydrogen, confer a more favorable pharmacokinetic profile relative to under-methoxylated counterparts [6–8]. In particular, NOB shows numerous protective effects, including metabolism-promoting, anti-inflammatory and anticancer activities [8–10]. As a chemopreventive agent, NOB exhibits antitumor effects against various cancer cells [11–17]. Interestingly, NOB also functions in a combination setting, acting to sensitize a paclitaxel-resistant A2780 ovarian cancer cell line to the chemotherapeutic agent [16], illustrating a safe and versatile natural compound that warrants further functional and mechanistic investigations.

¹Department of Biochemistry and Molecular Biology, McGovern Medical School, The University of Texas Health Science Center at Houston (UTHealth), Houston, TX 77030, USA.

²Center for Computational Systems Medicine, School of Biomedical Informatics, The University of Texas Health Science Center at Houston (UTHealth), Houston, TX 77030, USA.

³Department of Neurosurgery, McGovern Medical School, University of Texas Health Science Center at Houston (UTHealth), Houston, TX 77030, USA. ⁴Department of Pediatrics, Baylor College of Medicine, Houston, TX 77030, USA.

⁵Neurological Research Institute, Texas Children's Hospital, Houston, TX 77030, USA. ⁶Lester & Sue Smith Breast Center, Baylor College of Medicine, Houston, TX 77030, USA.

⁷Institute of Molecular Medicine, McGovern Medical School, University of Texas Health Science Center at Houston (UTHealth), Houston, TX 77030, USA. ✉email: seung-hee.yoo@uth.tmc.edu; zheng.chen.1@uth.tmc.edu

✉email: seung-hee.yoo@uth.tmc.edu; zheng.chen.1@uth.tmc.edu

Edited by Professor Stephen Tait

Received: 11 November 2021 Revised: 19 March 2022 Accepted: 4 April 2022

Published online: 19 April 2022

replating. Cells were harvested at 24 h Nobiletin treatment, and fixed in 70% ethanol overnight. DNA staining was performed with a solution of 20 µg/ml propidium iodide containing 10 µg/ml RNase A. Approximately 2×10^4 cells were analyzed by flow cytometry using a Cytomics FC500 flow cytometer running on CXP software (Beckman Coulter, Canada).

Western blot analysis

Western blotting was performed largely as described previously [45]. Briefly, cells were washed with cold PBS and lysed in HEPES lysis buffer. Protein extracts were separated by SDS polyacrylamide gel electrophoresis and blotted onto a nitrocellulose membrane. Blocking was performed at room temperature for 1 h in TBS-Tween 20 (TBS-T) with 5% blocker (Bio-Rad, CA, USA), followed by incubation with the primary antibodies diluted in TBS-T. After washing with TBS-T, the membrane was incubated with horseradish peroxidase-conjugated secondary antibodies. The protein bands were visualized using a West-Q Pico ECL solution (GenDEPOT). Primary antibodies against the following proteins were used: RORα (ab256799, Abcam); RORγ (sc-293150, Santa Cruz); IκBα, p65 and phospho-p65 (#9242, #4764, and #3033, Cell Signaling Technology, MA, USA); Flag (A8592), and GAPDH (Sigma). Original blot images are presented in the Supplementary Information.

Immunocytochemistry

MDA-MB-231 cells were plated and cultured on poly-D-lysine-coated glass coverslips in six-well plates. Twenty-four hours after transfection, the cells were treated with TNF-α (GenScript, NJ, USA) for 15 and 30 min. Then the cells were washed with cold PBS three times and fixed with 4% formaldehyde (Thermo Fisher, MA, USA) in PBS for 15 min at room temperature. They were then rinsed with cold PBS twice and permeabilized with PBS containing 0.1% Triton X-100 (Sigma) for 10 min at room temperature followed by washing with PBS three times. To block the nonspecific binding of the antibodies, samples were incubated with 3% BSA (Invitrogen) in PBS for 1 h at room temperature. Primary antibody against p65 (Cell Signaling Technology) was added to the samples and incubated for overnight at 4 °C. After washing with PBS three times, the cells were incubated with anti-rabbit secondary antibody conjugated with Alexa 488 (Invitrogen) for 1 h at room temperature followed by three times of PBS wash. Cells were stained with a DAPI (1 ng/ml; Sigma) for 5 min. Images were obtained with an LSM700 Confocal microscope (Carl Zeiss, Germany).

Luciferase reporter assay

MDA-MB-231 cells were seeded in 24-well plates. pGL4.32 [luc2P/NF-κB-RE/Hygro] Vector (Promega, WI, USA) and pSV-β-Galactosidase Control Vector (Promega) were co-transfected using Lipofectamine 2000 (Invitrogen). Cells were treated NOB at 10, 20, and 30 µM for 12 h. β-Galactosidase was used for normalization. All luciferase measurements were performed with the Luciferase Assay kit (Promega) using a Tecan Infinite M200 plate reader (TECAN Life Science).

Total RNA extraction and real-time quantitative PCR (qPCR) analysis

Real-time qPCR analysis was conducted as described [46] with minor modifications. Briefly, total RNA was isolated using the PureExtract RNAsol (GenDEPOT). Quantitative reverse transcriptase-PCR was used for determining the mRNA levels of each gene. First, cDNA was synthesized using the amfiRivert cDNA Synthesis Platinum Master Mix (GenDEPOT). The reverse transcription reaction mixture was incubated with the amfiSure SYBR Green qPCR Master Mix (GenDEPOT), followed by real-time amplification and quantitation in Mx3000P qPCR System (Agilent Genomics, CA, USA) according to the manufacturer's protocol. The fluorescence threshold value was calculated using the MxPro (Agilent Genomics). Data were processed with the comparative cycle threshold method and expressed as fold increase relative to the basal transcription level. Expression of target genes was calculated with the $2^{-\Delta\Delta Ct}$ method, using GAPDH as a reference. Primers for qPCR analysis are shown in Supplementary Table 1.

Chromatin immunoprecipitation (ChIP) assays

Cells were fixed in 1% formaldehyde for 10 min at room temperature and neutralized with 125 mmol/L glycine for 5 min. After washing with PBS, cell lysates were sonicated to produce chromatin fragments in 200–500 bp in

size. Fragmented chromatin was added into the ChIP dilution buffer (16.7 mM Tris-HCl (pH 8.1), 167 mM NaCl, 1.2 mM EDTA, 1.1% Triton X-100, 0.01% SDS, and inhibitor cocktail). Samples were incubated with anti-RORγ antibody (Santa Cruz, USA) at 4 °C. Immune complexes were precipitated with Protein A resin (Millipore Upstate, MA, USA) and were transferred to mini columns (Bio-Rad) for washing. Finally, the beads were eluted using TE buffer. DNA-protein cross-links were reversed by incubation with 10% Chelex at 95 °C for 10 min. The DNA was treated with proteinase K (Roche, Switzerland) at 55 °C for 30 min. Precipitated chromatin was used as the template for PCR. PCR was carried out using following primer pairs:

RORE1 (Forward 5'-TGGTGGTTGTGGATACCTTGC-3' and Reverse 5'-ACGATCCTTTTCTGCGGGA-3')

RORE2 (Forward 5'-GGCACCCAAATTCGAGGAGA-3' and Reverse 5'-GGCAGGATGGGACTACCTTG-3')

RORE3 (Forward 5'-ACTTGGTAGAATTGGTACAGGC-3' and Reverse 5'-ACAAGGCCAGTCAAGGTAAGA-3')

RNA-seq data analysis

For RNA-seq data analysis, MDA-MB-231 cells was treated 10 µM for 24 h. Total RNA was isolated using the PureExtract RNAsol (GenDEPOT). Two micrograms of extracted RNA samples were used for library construction and RNA-seq analysis (Novogene). The differentially expressed genes (DEGs), with thresholds of $p < 0.05$ and fold change > 2 , were screened by R package Limma 3.46 [47].

Gene ontology analysis of DEGs was implemented on the integrated platform DAVID [48]. Functional profiles of DEGs were analyzed and visualized by using ClusterProfiler 3.18.1 [49].

Xenograft studies

All mouse housing and experiments were performed in accordance with the Animal Welfare Committee at University of Texas Health Science Center. Four-week-old outbred female athymic nu/nu mice were obtained from the Jackson Laboratory (Bar Harbor, ME, USA). The mice were randomly divided into four groups and were injected subcutaneously with MDA-MB-231 cells (1×10^6). The five-week-old female FVB mice (Jackson Laboratory) were randomly divided into two groups and injected subcutaneously with DB7 cells (2×10^6). Each cell line was suspended in 50% DPBS/50% growth factor reduced matrigel (Corning, NY, USA) and injected into the abdominal mammary fat pad of nude mice or FVB mice.

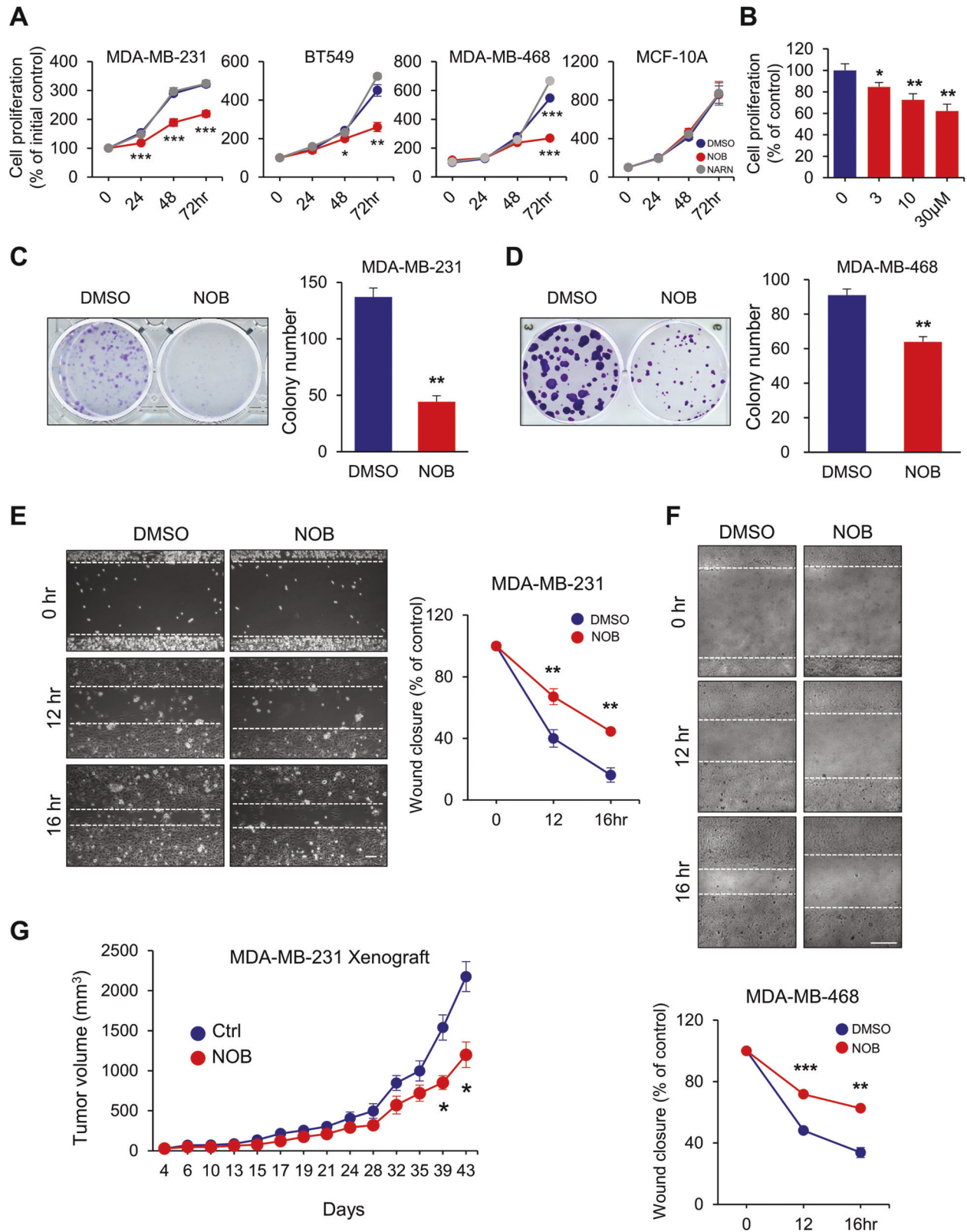
After tumor cells were injected, mice were fed with standard chow alone or standard chow supplemented with 0.1% NOB (10 mg/kg b.w.) for the duration of studies. For the combination treatment with DTX, when tumors reached the average size of 150–200 mm³, mice were randomized and control DMSO or DTX (10 mg/kg) was administered by intraperitoneal inject once a week for 4 weeks. Tumor volume (mm³) was measured for 43 days after injection of MDA-MB-231 or DB7 cells and calculated using the equation: tumor volume = length × (width)² × 0.5. At the end of the experiments, mice were sacrificed and tumor and plasma were dissected immediately. Interactions between drugs were presented as the combination index (CI), calculated by dividing the expected growth inhibition rate by the observed growth inhibition rate: CI < 1.0 indicates antagonistic cytotoxicity; CI = 1.0 is additive cytotoxicity; and CI > 1.0 is synergistic cytotoxicity.

TNF-α enzyme-linked immunosorbent assay (ELISA)

For ELISA assay, tumors were dissected immediately from euthanized mice after finishing experiment and stored at -80 °C. Frozen tumor samples were pulverized to get powder tumor. Powder tumor tissues were homogenized in lysis buffer in the presence of a cocktail of proteinase inhibitors (Sigma, MO, USA). Plasma was isolated from whole blood after centrifuge (3000 rpm for 15 min at 4 °C). TNF-α levels of tumor and plasma were detected using TNF-α ELISA kit (R&D Systems, MN, USA) according to the instructions from the manufacturer.

Immunofluorescence (IF)

Formalin-fixed, paraffin-embedded tumor tissue sections were stained with various antibody for IF. Briefly, the paraffin was removed by Histo-Clear (National Diagnostics, GA, USA). For hydration, the slides were dipped in a gradient of ethanol solution (from 100 to 30%) and in water for 15 min at room temperature. Next, the slides were placed in 0.01 M citric acid buffer (pH 6.0) at 95 °C for 30 min for antigen retrieval. The slides were blocked for 1 h with 5% of goat serum in order to prevent the nonspecific binding of the antibodies and then treated with different specific primary



antibodies: Ki67 (Abcam, Cambridge, UK), p-p65 (Cell Signaling, MA, USA), and F4/80 (eBioscience, CA, USA) for overnight at 4°C followed by incubation with the secondary antibodies (Alexa Fluor 488 goat anti-rabbit IgG (H + L) and goat anti-rat IgG2a-FITC (Invitrogen, CA, USA) for 1 h at room temperature). Nuclei were counter-stained by DAPI Fluor mount-G

(SouthernBiotech, AL, USA). Images were then captured at least four sections of each samples using a fluorescence microscope (Leica, Germany) and at least four different samples per each group were analyzed by ImageJ program using ImageJ (fluorescent intensity area/total image area × 100) in each experiment.

Fig. 1 NOB suppress cell survival and motility of TNBC. **A** TNBC cell lines (MDA-MB-231, BT549, and MDA-MB-468) and MCF10A were treated for 24, 48, and 72 h with 10 μ M NOB or 0.1% DMSO as control. Cell proliferation was determined by WST-1 assays. Data represent mean \pm SEM. Two-tailed Student's *t*-test shows significant statistical difference between DMSO and NOB. **p* < 0.05, ***p* < 0.01, and ****p* < 0.001. **B** MDA-MB-231 cells were treated with various concentrations of NOB (0–30 μ M) as indicated for 48 h and subjected to WST-1 assays. Data represent mean \pm SEM. Two-tailed Student's *t*-test, **p* < 0.05 and ***p* < 0.01 vs control. **C** NOB suppressed MDA-MB-231 colony formation. Right panel: quantification. Data represent mean \pm SEM. Two-tailed Student's *t*-test, ***p* < 0.01. **D** NOB suppressed MDA-MB-468 colony formation. Right panel: quantification. Data represent mean \pm SEM. Student *t*-test, ***p* < 0.01. **E** Wound-healing assay. The results are expressed as the percentage of motility compared with control cells at 0 h (100%). Data are shown as representative images or mean \pm SEM from three independent experiments. Two-tailed Student's *t*-test, ***p* < 0.01. Scale bar = 100 μ m. **F** Wound-healing assays as above. Data represent mean \pm SEM. Student's *t*-test, ***p* < 0.01, and ****p* < 0.001. Scale bar = 277.3 μ m. **G** Athymic nude mice were implanted with MDA-MB-231 by mammary fat pad injection. Tumor volume was measured regularly after treatment and the data shown are the mean tumor volumes \pm SEM (*n* = 5/group). Two-tailed Student's *t*-test, **p* < 0.05; Ctrl vs NOB.

Statistical analysis

Data are presented as mean \pm SEM unless otherwise indicated. All *n* numbers refer to biologically independent samples. Data were analyzed using Student's *t*-test, one-way, or two-way ANOVA with Tukey, Dunnett, and Sidak tests for multiple-group comparisons. A *p* value < 0.05 is considered to indicate statistical significance.

RESULTS

NOB suppresses TNBC cell growth and motility

Having identified the RORs as the direct target of NOB and given that ROR levels are broadly reduced in various cancer types [18, 35], we investigated a possible role of NOB–ROR against cancer. Screening of pancreatic, lung, and breast cancer cell lines identified three TNBC cell lines as highly sensitive to NOB (10 μ M) (Supplementary Fig. 1A and Fig. 1A). Specifically, NOB (10 μ M) significantly impeded the growth of MDA-MB-231, BT549, and MDA-MB-468 (Fig. 1A, 31.9%, 42.2%, and 50.9% reduction compared to DMSO at 72 h, respectively) without affecting the growth of MCF10A (normal breast epithelial cells) or MCF7 (ER/PR-positive breast cancer cells). In accordance, TCGA database search revealed that ROR expression was significantly reduced in TNBC (Supplementary Fig. 1B). Furthermore, NOB displayed progressive inhibition of MDA-MB-231 proliferation in a dose-dependent manner (Fig. 1B). Next, we examined ROR α / γ involvement by examining effects of a previously reported ROR α / γ agonist, SR1078 [50]. Similar to NOB, SR1078 was able to curtail MDA-MB-231 cell proliferation by 13.3% (*p* < 0.01) (Supplementary Fig. 1C).

Next, we performed clonogenic and wound-healing assays to assess effects of NOB on colony formation and motility of MDA-MB-231 and MDA-MB-468 cells. We observed that colony formation and colony size were markedly reduced by NOB after 10 days of treatment in MDA-MB-231 (Fig. 1C) and MDA-MB-468 (Fig. 1D) cells. As measured by migration distance, pretreatment of MDA-MB-231 and MDA-MB-468 cells with NOB strongly inhibited their motility (Fig. 1E, F).

Next, we performed xenograft experiments using athymic nude mice. Nude mice, implanted with MDA-MB-231 cells at the left inguinal mammary fat pad, were fed with regular diet (Ctrl) or NOB-containing (0.1%) (NOB) diet. The mean tumor volumes in the mice fed with NOB were significantly reduced to 1199.6 mm³ by day 43 compared to 2175.7 mm³ in the control mice (*p* < 0.05) (Fig. 1G). These results demonstrate that NOB effectively reduces TNBC cell growth both in vitro and in vivo.

TNBC cells do not exhibit circadian rhythms

Previously, NOB was found to prevent metabolic syndrome in a circadian clock-dependent manner [18]. Given the circadian dysregulation in tumor cells [51, 52], we investigated circadian rhythms in MDA-MB-231 and MDA-MB-468 cells by monitoring real-time bioluminescence from the introduced stable expression of the Bmal1::Luciferase and Per2::Luciferase (Supplementary Fig. 2A and B, respectively). Compared to the U2OS cells as a positive

control, we observed no persistent circadian bioluminescence rhythm, regardless of DMSO or NOB treatment. This agrees with a previous study showing severely disruption of circadian oscillation in MDA-MB-231 cells [53]. The lack of sustained circadian rhythms in MDA-MB-231 cells suggest that the inhibitory effects of NOB may be more directly related to RORs (ROR α and ROR γ) [39, 54–58], rather than the clock machinery.

NOB inhibits MDA-MB-231 cell growth via an ROR-dependent mechanism

Next, we performed loss-of-function experiments by examining cell viability in MDA-MB-231 cells harboring CRISPR-Cas9 sgRNA-mediated *RORA/C* knockdown (Supplementary Fig. 3A). Interestingly, respective ROR knockdown appeared to have reciprocal effects to diminish the level of the other ROR, with a more significant reduction in ROR α levels from *RORC* knockdown (Supplementary Fig. 3B). As shown in Fig. 2A, *RORA/C* knockdown increased cell proliferation. NOB showed much diminished cytotoxic effects on *ROR* knockdown cells (*p* < 0.01 for *RORA* knockdown and *p* < 0.05 for *RORC* knockdown cells) in comparison with WT MDA-MB-231 cells where NOB was able to significantly reduce cell proliferation after 48 and 72 h of treatment, demonstrating the ROR dependence of NOB anti-TNBC effects. In accordance, I κ B α induction by NOB was abrogated by *ROR* knockdown (Fig. 2B).

MDA-MB-231 cells, treated with NOB (10 or 20 μ M) or Doxorubicin (DOX) 10 μ g/ml, were stained with TUNEL and DAPI (Fig. 2C). While DOX-treated cells showed positive TUNEL staining, NOB-treated cells did not. We next evaluated caspase-3/7 activation, and observed significantly increased caspase activation in DOX-treated, but not NOB-treated, cells (Fig. 2D). These results suggest that NOB does not trigger apoptosis in MDA-MB-231 cells. We further examined cell cycle effects of RORs by flow cytometry. NOB treatment significantly increased cell cycle arrest at the G2/M phase (Fig. 2E). In contrast, there is no significant cell cycle effect after siRNA-mediated *ROR* knockdown (Supplementary Fig. 3C), suggesting a role of NOB–ROR in the G2/M checkpoint.

We next generated *RORA* or *RORC* overexpressing MDA-MB-231 clones (*RORA*:231 and *RORC*:231). Expression of ROR α or ROR γ was confirmed by qPCR and western blotting (Supplementary Fig. 3D and E respectively). NOB inhibited cell proliferation dose-dependently in MDA-MB-231 cells transfected with the empty vector (P3Xflag-CMV10-Neo^r) (Supplementary Fig. 3F). Both *RORA* and *RORC* expression significantly decreased MDA-MB-231 proliferation compared to the control (Fig. 3A, *p* < 0.001 for all at 72 h), and NOB further reduced proliferation of MDA-MB-231 cells expressing *RORA* or *RORC* (*p* < 0.001 for all at 72 h). *RORA* or *RORC* expression also significantly decreased cell motility (Fig. 3B) and colony formation (more significantly by *RORC*, Fig. 3C) compared to control cells. Importantly, NOB displayed strong effects in these ROR-expressing cells, highlighting a prominent role of the NOB–ROR axis against TNBC cells.

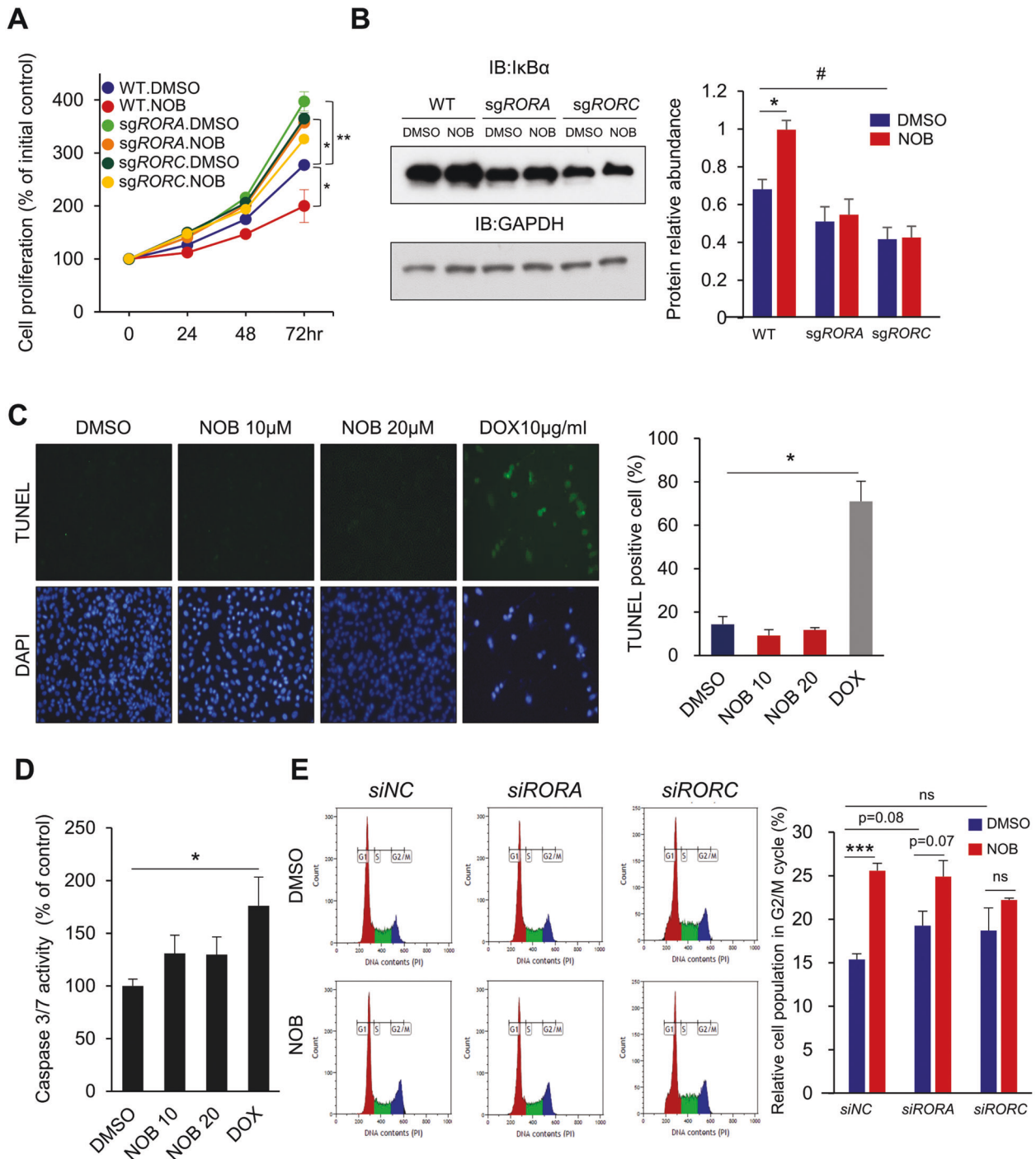


Fig. 2 ROR-dependent cell growth is inhibited by NOB. **A** WT and derivative MDA-MB-231 cells with *RORA* or *RORC* knockdown were treated with 10 μ M NOB for 24, 48, and 72 h. The data represent mean \pm SEM. Two-way ANOVA with Tukey's multiple comparison, $*p < 0.05$; $***p < 0.01$. **B** I κ B α protein expression in the above ROR knockdown cells treated with DMSO or 10 μ M NOB for 24 h. Right panel: quantification from four experiments. Data represent mean \pm SEM. Two-way ANOVA with Sidak's multiple comparisons test, $*p < 0.05$, and two-tailed Student's *t*-test, $^{\#}p < 0.05$ WT.DMSO vs sgRORC.DMSO. **C** MDA-MB-231 cells were treated with NOB or Doxorubicin (DOX) for 24 h and then stained with TUNEL and DAPI. Two-tailed Student's *t*-test, $*p < 0.05$. **D** MDA-MB-231 cells were treated with NOB (10 or 20 μ M) or DOX, and apoptosis was examined by detecting caspase-3/7 activity. Data represent the mean \pm SEM of three experiments. Two-tailed Student's *t*-test, $*p < 0.05$. **E** MDA-MB-231 cells were transfected with control siRNA, siRORA, or siRORC and treated with 10 μ M NOB for 24 h. Right panel: quantification data are presented as the percentage of the corresponding phase of the cells and the mean \pm SEM. Two-tailed Student's *t*-test, $***p < 0.001$.

I κ B α and NF- κ B signaling are direct targets of the NOB-ROR axis

Next, we investigated the molecular mechanism underlying NOB effects in MDA-MB-231 cells. Previous studies have identified I κ B α , encoded by *NFKBIA*, as a direct transcriptional target of ROR α [59].

I κ B α is a pivotal regulator of NF- κ B signaling [60, 61]. Furthermore, TCGA database analysis showed a significant correlation of *NFKBIA* and *RORC* expression in breast cancer (Supplementary Fig. 4A), suggesting a regulatory role of RORs in I κ B α transcription regulation. To determine whether I κ B α transcription is responsive

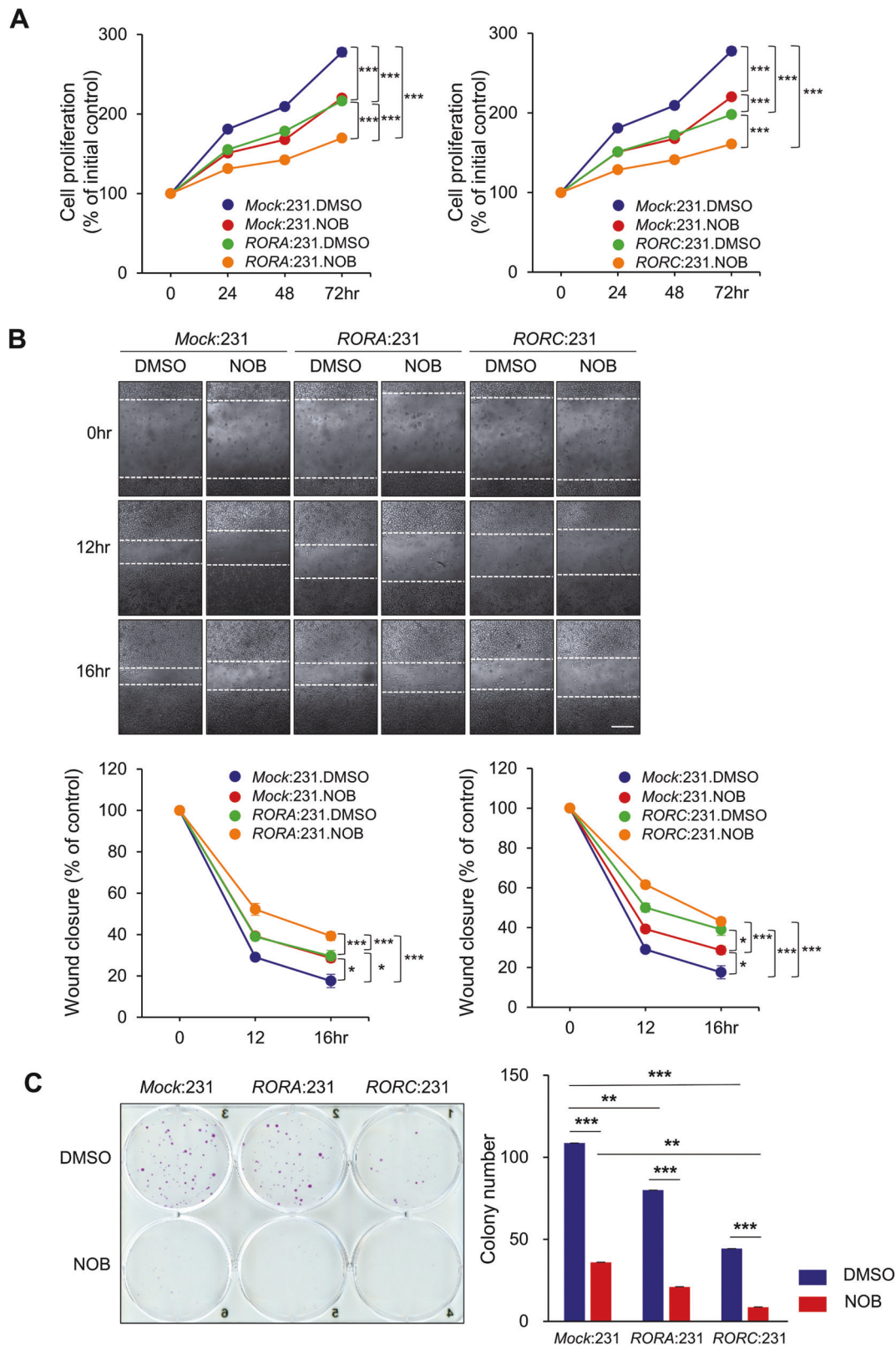
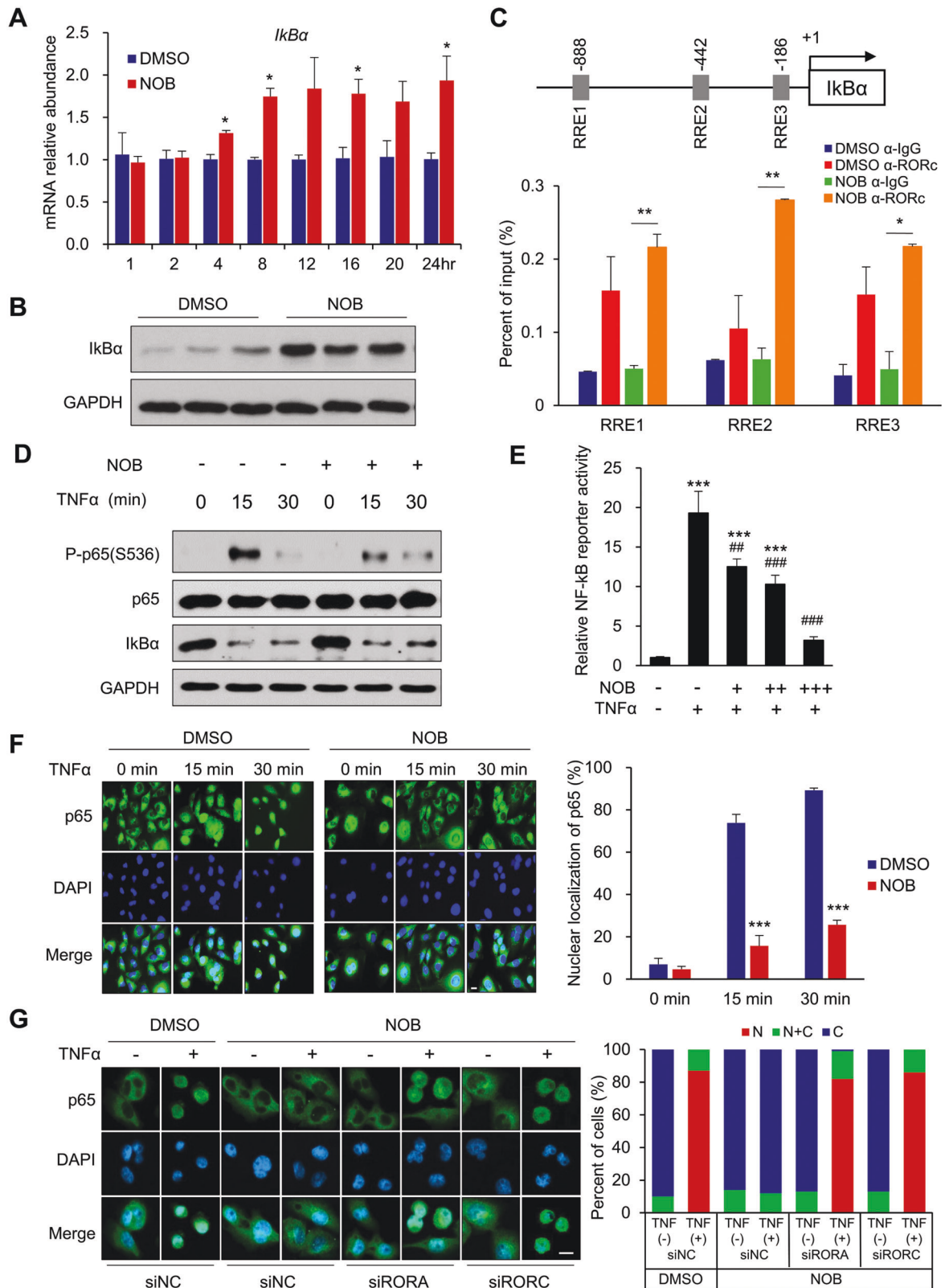


Fig. 3 Combination of NOB and ROR ectopic expression in MDA-MB-231 cells suppresses cell growth and motility. **A** WST-1 assays. Mock indicates P3Xflag-CMV10-Neo^r (Empty vector). Data represent mean \pm SEM. Two-way ANOVA with Sidak's multiple comparisons test showed significant difference. *** p < 0.001. **B** Wound healing assays showed retarded motility in *RORA*- or *RORC*-expressing MDA-MB-231 cells. The results were expressed as the percentage of the motility of the control cells (100%, upper panel) ($\times 100$ magnification, scale bar = 277.3 μ m). Data represent mean \pm SEM. Two-way ANOVA with Sidak's multiple comparisons, * p < 0.05 and *** p < 0.001. **C** NOB and *RORA/C* expression in MDA-MB-231 showed a combination effect in colony formation assays. Right panel: quantification. Data represent mean \pm SEM. Two-way ANOVA with Sidak's multiple comparisons test, ** p < 0.01 and *** p < 0.001. Interaction between *RORA/C* expression and NOB, p = 0.0026 via two-way ANOVA.



to NOB in MDA-MB-231, we performed qPCR analysis (Fig. 4A) which showed that *IkBa* mRNA expression was activated by NOB. We next examined *IkBa* protein expression in response to NOB. In MDA-MB-231 cells treated with NOB, *IkBa* proteins were strongly induced (Fig. 4B).

We determined whether NOB facilitates ROR binding to the consensus ROR response elements (RRE) of the *IkBa* promoter. Based on TRANSFAC analysis (<http://genexplan.com/transfac/>), we identified three putative RRE sites (Fig. 4C). MDA-MB-231 cells treated 20 μ M NOB for 12 h were collected, and chromatin

Fig. 4 The NF- κ B pathway is a direct target of the NOB–RORs axis. **A** MDA-MB-231 cells were treated with NOB. *IkB α* mRNA expression was measured by qRT-PCR. Data represent mean \pm SEM. Two-tailed Student's *t*-test, $*p < 0.05$. **B** MDA-MB-231 cells were treated with NOB for 24 h. *IkB α* protein expression was measured by western blotting. In all, 4.4-fold change, $p < 0.01$ compared to DMSO. **C** Schematic representation of putative RRE sites found in the *IkB α* promoter (TRANSFAC). The distance in bp from the transcription start site of *IkB α* gene is shown. MDA-MB-231 cells were treated with 20 μ M NOB for 12 h. Samples were normalized to input chromatin and expressed as % input. Error bars represent mean \pm SD; $n = 2$; two-tailed Student's *t*-test. $*p < 0.05$; $**p < 0.01$. **D** MDA-MB-231 cells were treated with 10 μ M NOB for 12 h prior to TNF- α treatment (10 ng/ml). Whole-cell lysates were subjected to western blot analysis using anti-*IkB α* , phospho-p65 (Ser536), total p65, and GAPDH antibodies. **E** MDA-MB-231 cells were transfected with pGL4.32 [Luc2P/NF- κ B-RE/Hygro] vector and treated with NOB (+, 10 μ M; ++, 20 μ M; +++, 30 μ M) for 12 h prior to TNF- α treatment. Data represent mean \pm SEM. Two-tailed Student's *t*-test, $***p < 0.001$. Compared with the TNF- α control, $##p < 0.01$, $###p < 0.001$. **F** p65 nuclear localization by TNF- α was inhibited by NOB in MDA-MB-231. Representative immunofluorescence images of endogenous p65 in MDA-MB-231 with NOB pretreatment 12 h prior to TNF- α treatment ($\times 400$ magnification, scale bar = 10 μ m). Two-tailed Student's *t*-test, $***p < 0.001$. **G** MDA-MB-231 cells were transfected with control siRNA, siRORA or siRORC and treated 10 μ M NOB for 12 h prior to TNF- α treatment. Representative confocal images are shown ($\times 400$ magnification, scale bar = 10 μ m). Cell extracts were subjected to dual luciferase assays. N nucleus; C cytoplasm.

immunoprecipitation (ChIP) was performed by using IgG or anti-ROR γ antibody. qPCR amplification revealed that RRE1, RRE2, and RRE3 showed NOB-dependent ROR γ recruitment (two-tailed Student's *t*-test: $*p < 0.05$; $**p < 0.01$). These results suggest these RRE elements are functionally involved in ROR binding.

NOB–ROR represses TNF- α -induced NF- κ B activation in MDA-MB-231 cells

To examine the mechanistic role of NOB–ROR in NF- κ B signaling in TNBC, we treated MDA-MB-231 cells with NOB (10 μ M for 12 h) followed by treatment of tumor necrosis factor α (TNF- α ; 10 ng/ml) for 15 and 30 min. Immunoblotting analysis showed that NOB treatment significantly attenuated levels of phospho-p65 (Ser536) after 15 min of TNF- α treatment (Fig. 4D and Fig. S4B). In accordance, in NF- κ B reporter assays using MDA-MB-231 cells transfected with an NRE-luciferase reporter, NOB dose-dependently reduced NF- κ B transcriptional activity upon TNF- α induction (10 ng/ml) (Fig. 4E). We next investigated NOB effects on p65 nuclear localization. TNF- α treatment strongly induced endogenous p65 nuclear localization which was inhibited by NOB pretreatment (Fig. 4F).

To investigate the role of RORs in NF- κ B signaling, MDA-MB-231 cells were transfected with control siRNA, si-RORA, or si-RORC and treated with NOB (10 μ M) for 12 h. While NOB strongly inhibited NF- κ B nuclear localization in control siRNA-treated cells, *Ror* knockdown abrogated the NOB effect on p65 nuclear localization in response to TNF- α (Fig. 4G). These results therefore indicate a novel role of ROR–NOB to regulate NF- κ B signaling via p65 nuclear localization.

Inducible p65 expression abolishes NOB inhibition of MDA-MB-231 growth

Next, we employed a tet-on system [62, 63] to generate inducible p65 expressing MDA-MB-231 cells (Fig. 5A and Supplementary Fig. 4C). Cell proliferation assays using control and p65-inducible cells showed that p65 induction abolished NOB effects on cell proliferation and motility. Whereas NOB significantly reduced cell proliferation, p65 induction abolished NOB effects on cell proliferation (Fig. 5B) and motility (Fig. 5C and Supplementary Fig. 4D). Consistently, colony formation assay showed p65 induction bypassed NOB effects (Fig. 5D). As expected, *IkB α* protein induction by NOB was disrupted by p65 overexpression (Supplementary Fig. 4E). qPCR analysis further revealed that expression of multiple p65 target genes in cell proliferation and Wnt/ β -catenin signaling was downregulated by NOB, which was abolished in cells overexpressing p65 (Supplementary Fig. 4F). These results suggest that p65 overexpression counteracts NOB to regulate tumor cell proliferation and motility, providing important mechanistic evidence linking NOB–ROR and NF- κ B signaling.

Regulation of cancer and NF- κ B pathways in TNBC tumors by NOB–ROR

To delineate changes in the gene expression landscape by NOB in MDA-MB-231 cells, we performed RNA-seq using MDA-MB-231

treated with 10 μ M NOB for 24 h and identified large numbers of significantly differentially expressed genes (DEGs; >2 -fold change) in response to NOB treatment (Fig. 5E, F). As shown by Volcano plot (Fig. 5E) and pie chart (Fig. 5F), 2660 and 2277 genes were down- and up-regulated by NOB, respectively. Gene ontology analysis showed enrichment of a number of cancer-related cellular pathways, including metabolism/mitochondria, growth and translation, and importantly NF- κ B signaling (Fig. 4G–I). By cross-checking the GEO database, we further identified overlapping genes between our differentially expressed genes (DEGs) and reported ROR γ target genes in TNBC cells [64] (Supplementary Fig. 5A). These results are consistent with our previous finding linking NOB and mitochondria [19], on the other hand also underscore a pivotal function of NOB–ROR to target the NF- κ B pathway in TNBC cells. Of note, *IkB α* expression was induced by NOB in RNA-seq analysis (fold change = 1.59, $p = 0.01$), consistent with qPCR validation (fold change = 1.62, $p < 0.05$) (Supplementary Fig. 5B).

Combination of NOB with docetaxel (DTX) or carboplatin (CAR) inhibits TNBC cell growth

To assess the combination efficacy of NOB with a primary chemotherapy, we performed combination treatment of NOB with DTX or CAR and measured MDA-MB-231 cell proliferation. Interestingly, NOB and DTX showed robust combination efficacy (interaction $p < 0.01$ via two-way ANOVA), displaying superior inhibiting effects compared to DTX or CAR alone (Fig. 6A, B). These results suggest that NOB can serve as a strong enhancer for the primary chemotherapy drug.

We further investigated the enhancer effect of NOB in human MDA-MB-468 breast cancer cells and mouse DB7 breast cancer cells. As a control, NOB at 50 and 100 μ M doses exhibited no cytotoxicity on MCF10A cells after 48 h of treatment (Supplementary Fig. 6A). In MDA-MB-468 cells, the combination treatment of NOB (100 μ M) and DTX (5 nM) for 48 h strongly increased cell death by 69.2% and 77.5% compared to NOB and DTX respectively (Fig. 6C). In comparison, NOB at 50 μ M also showed a combination effect with 2.5 nM DTX, albeit to a lesser degree (Supplementary Fig. 6B). In DB7 cells, cell proliferation was attenuated dose-dependently by NOB (Fig. 6D, left), and at the lower doses tested (20 and 40 μ M), we detected a significant interaction effect (2-way ANOVA) between NOB and DTX (Fig. 6D). Moreover, the combination treatment of NOB at a high dose (100 μ M) and DTX (2.5 nM) further reduced cell proliferation by 32.1% and 36.5% compared to NOB and DTX respectively (Supplementary Fig. 6C). These results are consistent with those in MDA-MB-231 cells, suggesting a NOB function as a chemotherapy drug in TNBC.

Synergistic antitumor effect of NOB in combination therapy

Finally, we tested the in vivo efficacy of the combination of DTX and NOB in mice bearing orthotopic MDA-MB-231 xenografts. Consistent with Fig. 1G, tumor growth was significantly retarded by NOB

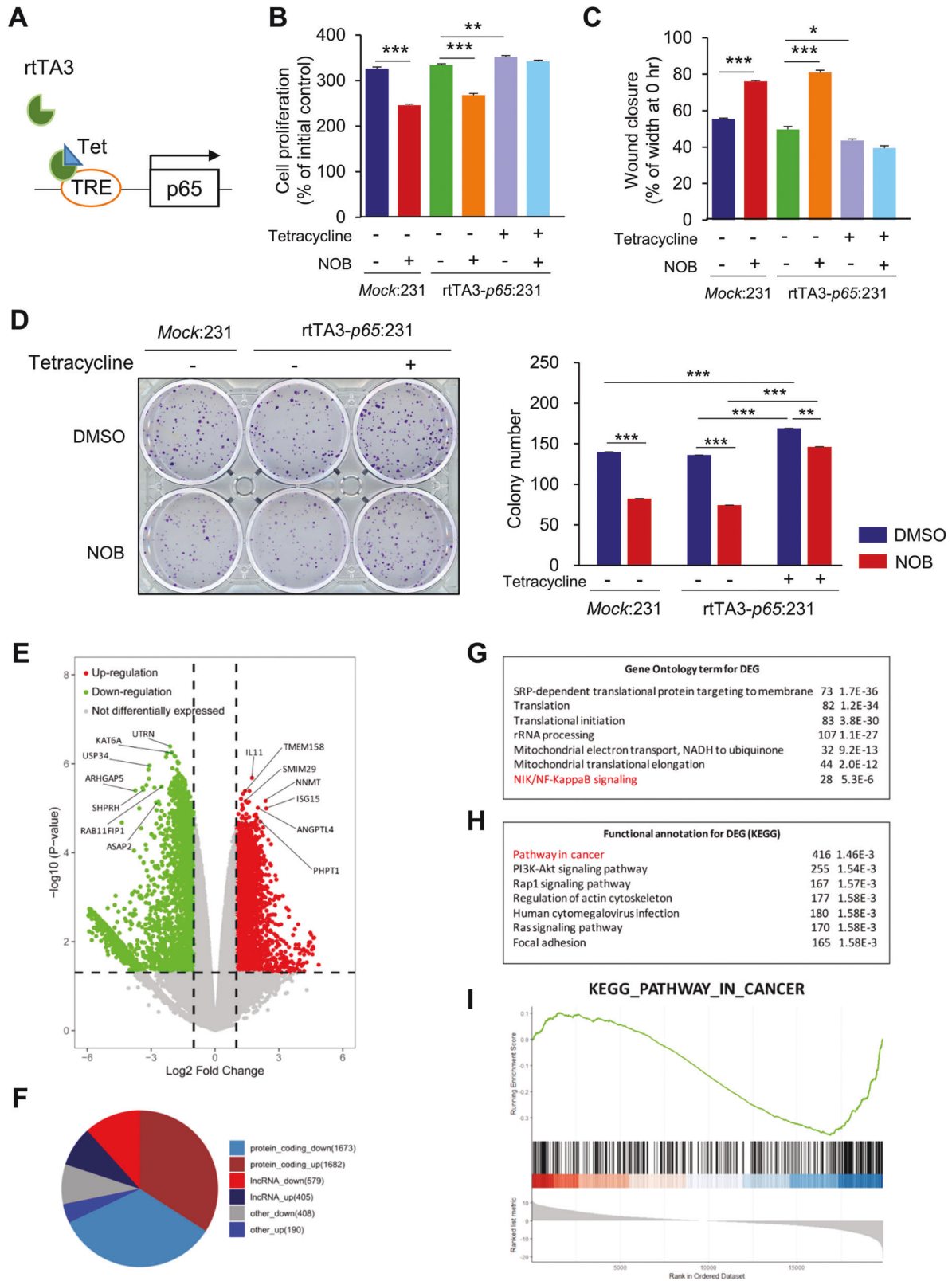


(Fig. 7A). DTX (indicated by arrow) alone significantly reduced tumor. Importantly, the DTX.NOB group showed the lowest tumor volume, with 73.5% reduction compared to the Ctrl and 36.2% compared to DTX alone ($p < 0.05$). In addition, the CI indicated the co-treatment of NOB and DTX shows synergistic effects on tumor

growth inhibition (CI = 1.22; Supplementary Table 2). These findings suggested that the combination treatment of DTX and NOB might be a novel treatment strategy for TNBC patients.

TNF- α is highly increased in breast cancer, and its expression significantly correlated with the migration, invasion, and

Fig. 5 p65 is targeted by NOB to inhibit TNBC. **A** Diagram indicating the p65-inducible system. **B** MDA-MB-231 cells were grown to confluence and treated NOB with (20 μ M) and tetracycline (100 nM) for 12 h. WST-1 assays were performed at 72 h after NOB treatment. Mock indicates pCW 57.1 vector (Empty template vector). Data represent mean \pm SEM. Two-way ANOVA with Sidak's multiple comparisons test, ** $p < 0.01$, and *** $p < 0.001$. **C** Wound-healing assay. The closure of wounds in MDA-MB-231 cells after 16 h of p65 induction by tetracycline (100 nM). The results are presented as relative motility to the width at 0 h (100%). Data represent mean \pm SEM. Two-way ANOVA with Sidak's multiple comparisons test, * $p < 0.05$ and *** $p < 0.001$. **D** Colony formation assays were performed with 20 μ M NOB. Data represent mean \pm SEM. Two-way ANOVA with Sidak's multiple comparisons test. ** $p < 0.01$ and *** $p < 0.001$. **E–I** RNA-seq analysis. **E** Volcano plot of 4937 differential expressed genes (DEGs) between DMSO and NOB treatment MDA-MB-231 cells ($p < 0.05$ and fold change > 2). Plots highlighted with red and green represent up- and downregulated genes. Multiple NF- κ B pathway genes are marked. **F** Pie chart of protein-coding genes, lncRNA, and other genes in the DEG set. **G** Gene ontology analysis of DEGs with DAVID. Top-ranked pathways are presented, including NF- κ B signaling indicated with red. **H** KEGG analysis of DEGs with ClusterProfiler. Top-ranked pathways are presented, including "Pathway in cancer". **I** Gene set enrichment analysis demonstrated the enrichment of gene sets related to cancer.

metastasis of breast cancer cells [65]. Since NF- κ B activation induces TNF- α secretion, we measured TNF- α levels from plasma and tumor tissues. NOB and DTX reduced TNF- α in plasma and tumors compared to Ctrl. In particular, the TNF- α level was most significantly reduced by the DTX.NOB combination ($p < 0.05$) (Fig. 7B). Immunostaining of the proliferation marker Ki67 showed that, compared to the control, NOB alone reduced Ki67 level by 57.3% and the DTX.NOB combination by 93.3%, suggesting NOB markedly increases the efficacy of DTX (Fig. 7C). Consistent with cell line results (Fig. 4F, G), immunostaining showed strong reduction of p-p65 by NOB, and there is a combination effect in the DTX.NOB group ($p < 0.05$ compared to DTX.Ctrl) (Fig. 7D).

While TNF- α has been implicated breast cancer growth, it may also function in the development of antitumor immune response [66]. Therefore, we tested antitumor efficacy of NOB in a syngeneic xenograft model using DB7 cells in immune-competent mice. On day 29, the average tumor volume of the NOB group was reduced by 42.4% compared to Ctrl (Supplementary Fig. 7A). The TNF- α levels of plasma (65.8% vs Ctrl) and tumor (66.9% vs Ctrl) were significantly decreased by NOB (Supplementary Fig. 7B). NOB treatment significantly reduced Ki67 and p-p65 levels by 86.6% and 75.4%, respectively, relative to the control (Supplementary Fig. 7C, D). These results illustrate a strong anti-TNBC effect of NOB, alone or in combination, in cells and in vivo.

DISCUSSION

We demonstrate that ROR activation by NOB is effective at limiting TNBC cell growth in vitro as well as in xenografts, and NOB shows a synergistic effect with chemotherapeutic drugs, particularly DTX. Molecular studies reveal that NOB-ROR reduces tumor proliferation and inflammation responses via downregulating TNF- α activity and p65 nuclear localization in TNBC, and gain-of-function evidence demonstrates a requisite role of NOB repression of p65 against TNBC. Our study highlights a novel target and strategy for TNBC treatment and reveals the cellular mechanism underlying the anticancer effect of NOB.

While PMFs are generally well tolerated [6], their cellular mechanisms often are not well understood. We previously identified ROR as a direct, high-affinity target of NOB [18]. Building on this finding, we report here TNBC as a specific, sensitive target for the NOB-ROR axis, and identified I κ B α /NF- κ B as a key cellular pathway. We show that NOB was able to inhibit cell cycle progression and motility of TNBC cells in vitro, consistent with growth inhibitory effects of NOB against cancer cells [10, 15, 67]. Importantly, the observed effects were dependent on RORs, providing an important functional validation of the NOB-ROR axis [18, 19]. Consistent with our previous study [19], individual ROR knockdown was able to significantly inhibit NOB effects, perhaps due to reciprocal regulation between the RORs via RORE or other promoter elements [25, 42, 68]. Consistent with a previous study [59], we also demonstrate a direct transcriptional regulation of NOB-ROR on the I κ B promoter and a role of NOB-ROR to suppress TNF- α induced p65 phosphorylation and

nuclear localization (see below). These results together provide significant mechanistic insights for a NOB-ROR axis impinging on cancer and inflammation.

The role of NF- κ B in tumorigenesis is well established [60, 61]. For example, the RelA/p65 NF- κ B subunit is responsible for the transactivation of downstream genes involved in the modulations of cell cycle distribution, cell survival, and apoptosis [69]. In accordance, p65 activation is an important sign of resistance to neoadjuvant chemotherapy in breast cancer patients [70]. Particularly for TNBC, p65 overexpression induced NF- κ B transcriptional activity and inhibited apoptosis triggered by celecoxib, a selective cyclooxygenase (COX)-2 inhibitor, in MDA-MB-231 cells [71]. Here, overexpression of p65 abolished the NOB effect on MDA-MB-231 cell proliferation and motility, providing important evidence that repression of NF- κ B signaling is required for the anticancer effect of NOB. TNF- α upregulation of the NF- κ B pathway is a major regulatory step for inflammation, including in the tumor microenvironment [72]. Here, we found that NOB dampened TNF- α -induced p65 phosphorylation and NF- κ B nuclear localization in MDA-MB-231 cells and xenograft tumors. Previously, ROR α overexpression abrogated glioma tumorigenesis through reducing TNF- α -mediated NF- κ B signaling [73]. Consistently, we show that ROR overexpression inhibited proliferation and motility in MDA-MB-231 cells, which was further enhanced by NOB.

TNBC is heterogeneous and only a subset of patients responds favorably to standard chemotherapy [1, 4]. While combination of chemo- and radio-therapy is the current standard treatment options for TNBC, there is an urgent need for new targets and therapeutic strategies including combination therapies. DTX has been employed in a combination therapy with JMR-231, a growth hormone-releasing hormone (GHRH) antagonist, which reduced tumor growth by 71.6% in MDA-MB-231 xenograft mice [74]. Here, we revealed an ROR-dependent mechanism suppressing NF- κ B signaling for a specific anti-TNBC effect of NOB, a promising chemopreventive agent. Importantly, in vitro and xenograft studies revealed superior antitumor efficacies by the DTX.NOB combination compared to NOB or DTX alone, which correlated with a similar effect to attenuate TNF- α levels in plasma and tumors. Our study is consistent with a previous study where NOB enhanced efficacies of several chemotherapeutic drugs including DTX against cancer cells that have acquired multidrug resistance [16]. Together, our results highlight a potential role of NOB as an anticancer agent, by itself or in combination.

A number of studies have illustrated functional interactions between NF- κ B signaling and circadian clocks [75–78]. However, while our initial studies identified NOB as a circadian clock-enhancing compound targeting RORs [18, 79], MDA-MB-231 cells did not display sustained circadian rhythms, consistent with other results [53]. Previously, we showed that preventive efficacies of NOB against metabolic disorders requires a functional circadian clock [18]. Whereas clock gene expression has been detected in TNBC, its expression levels tend to be dysregulated, including

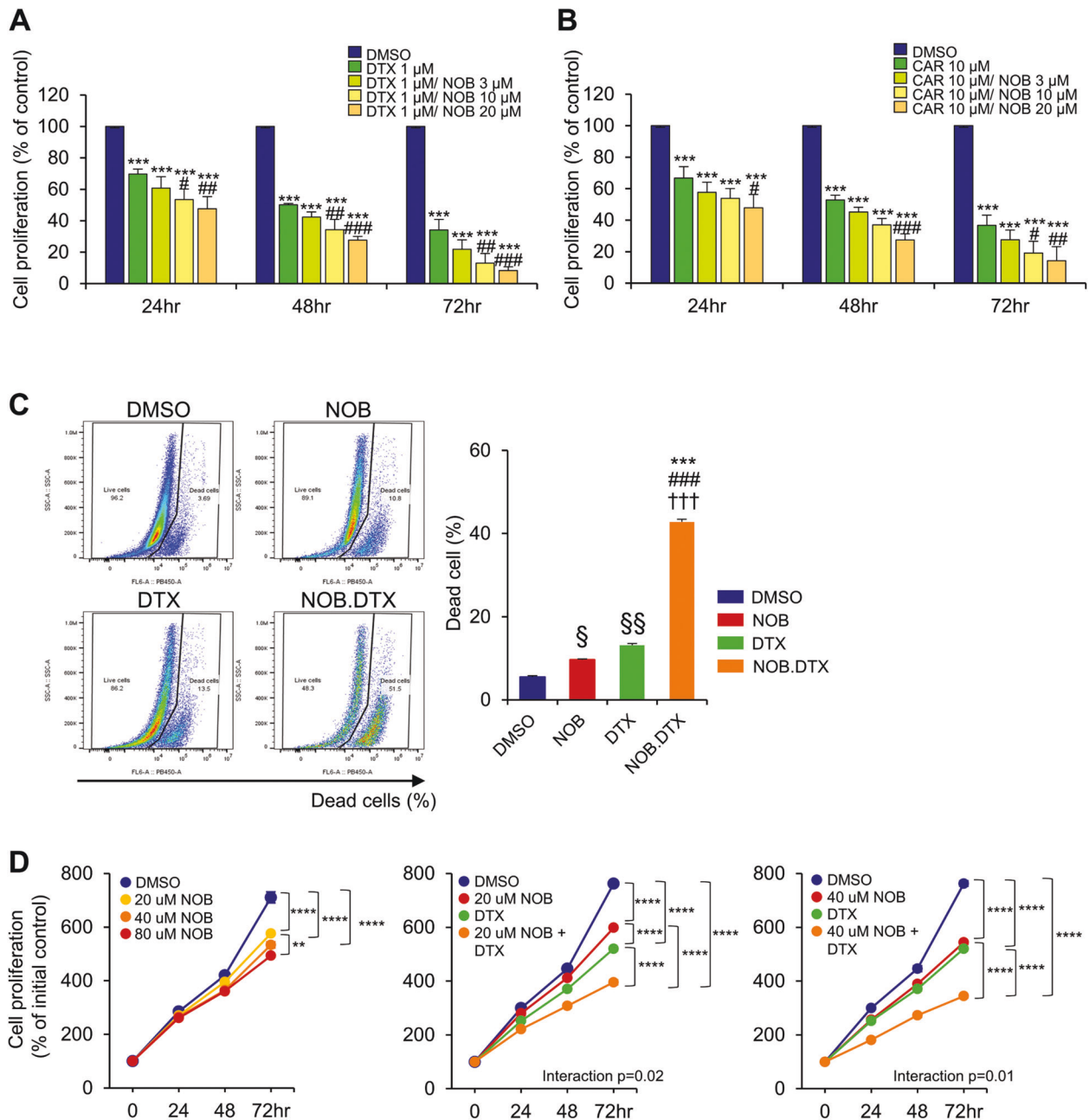


Fig. 6 Combination studies show the efficacy of NOB with DTX or CAR in TNBC cells. **A** MDA-MB-231 cells were treated with the NOB and/or DTX for 24, 48, and 72 h and cell proliferation was determined by WST-1 assays. Data represent mean \pm SEM. One-way ANOVA with Tukey's post hoc test showed significant difference compared to DMSO, $***p < 0.001$, compared to DTX, $^{\#}p < 0.05$, $^{\#\#}p < 0.01$, and $^{\#\#\#}p < 0.001$. Interaction, $p < 0.01$ via two-way ANOVA. **B** MDA-MB-231 cells were treated with NOB and/or CAR for 24, 48, and 72 h and cell proliferation was determined by WST-1 assay. Data represent mean \pm SEM. Two-tailed Student's *t*-test showed significant difference compared to DMSO, $***p < 0.001$, compared to CAR 10 μ M, $^{\#}p < 0.05$, $^{\#\#}p < 0.01$, and $^{\#\#\#}p < 0.001$. **C** MDA-MB-468 cells were treated with NOB (100 μ M) and/or DTX (5 nM) for 48 h and cell death was determined by FACS analysis. Left panel; Representative images of flow cytometric analysis; right panel; quantification. Data represent mean \pm SEM. Two-way ANOVA with Tukey's multiple comparisons test showed significant difference compared to DMSO, $***p < 0.001$, NOB, $^{\#\#\#}p < 0.001$, and compared to DTX, $^{\dagger\dagger\dagger}p < 0.001$ (interaction, $p < 0.001$ via two-way ANOVA). Student *t*-test compared to DMSO, $^{\S}p < 0.05$, $^{\S\S}p < 0.01$. **D** DB7 cells were treated with NOB (20, 40, and 80 μ M) and/or DTX (2.5 nM) for 24 and 72 h and cell proliferation was determined by WST-1 assays. Data represent mean \pm SEM. Two-way ANOVA with Tukey's multiple comparisons test showed significant difference compared to DMSO, $^{**}p < 0.01$, $^{****}p < 0.0001$.

RORs [51, 53, 80]. NOB appeared not to have rejuvenated circadian rhythms in MDA-MB-231 cells, suggesting that the NOB effect is mediated by RORs in a clock-independent manner [26, 27]. However, it remains to be investigated whether ROR activation by NOB intersects with cellular pathways that may require individual

clock components present in arrhythmic TNBC cells. In that regard, it is interesting to note that NOB inhibition of xenografts is greater in immune-competent host mice than in nude mice (Supplementary Fig. 7A vs Fig. 7A). Future studies should examine whether the systemic NOB effects on the host, including circadian rhythms and

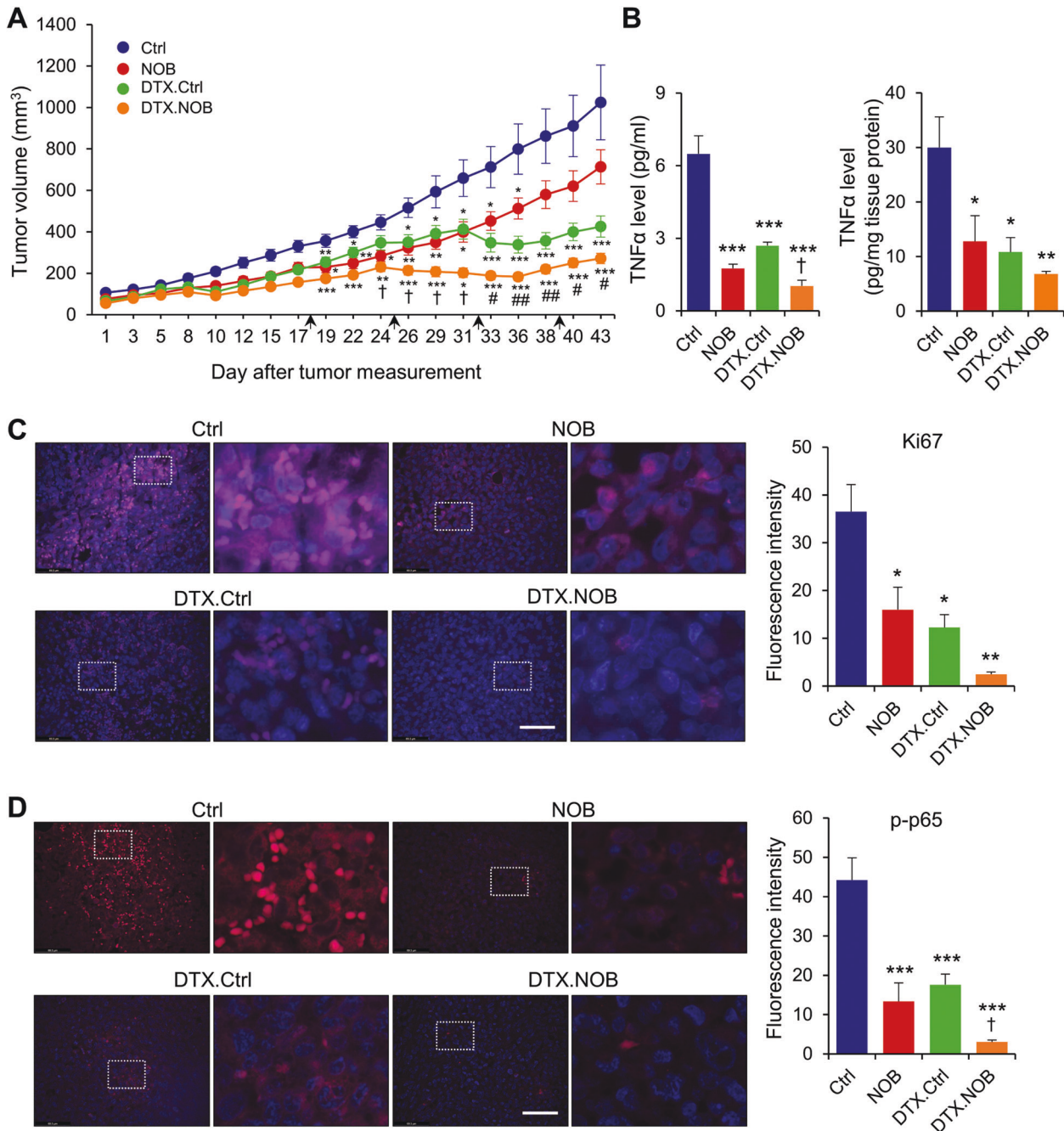


Fig. 7 NOB suppresses tumorigenesis in MDA-MB-231 xenograft mice. **A** DTX and NOB showed synergistic inhibitory effects in MDA-MB-231 xenograft tumor growth ($n = 6$ for Ctrl and NOB, $n = 7$ for DTX.Ctrl, and $n = 8$ for DTX.NOB). The black arrows show DTX injection time point (18, 25, 32, 39 days). Data represent mean \pm SEM. Two-way ANOVA with Tukey's multiple comparisons test showed significant difference compared to Ctrl, * $p < 0.05$, ** $p < 0.01$, and *** $p < 0.001$, compared with NOB, # $p < 0.05$ and ## $p < 0.01$, and compared with DTX.Ctrl, † $p < 0.05$, CI = 1.22. **B** TNF- α levels in plasma (left panel) and tumor (right panel) of MDA-MB-231 xenograft mice model. Data represent mean \pm SEM. Two-way ANOVA with Tukey's multiple comparisons test showed significant difference compared to Ctrl, * $p < 0.05$, ** $p < 0.01$, and *** $p < 0.001$ and compared to DTX.Ctrl, † $p < 0.05$. **C** Representative immunofluorescence images of the Ki67 (pink) and DAPI (blue) ($\times 400$ magnification, scale bar = 69.3 μ m). Quantitative analysis of the percentage of Ki67 immunoreactive area. Data represent mean \pm SEM. Two-way ANOVA with Tukey's multiple comparisons test, * $p < 0.05$ and ** $p < 0.01$. **D** Representative immunofluorescence images of the p-p65 (pink) and DAPI (blue) staining from representative images of the p-p65 (red) and DAPI (blue) immunofluorescence in the lesion area ($\times 400$ magnification, scale bar = 69.3 μ m). Quantitative analysis of the percentage of p-p65 immunoreactive area. Data represent mean \pm SEM. Two-way ANOVA with Tukey's multiple comparisons test showed significant difference compared to Ctrl, *** $p < 0.001$ and compared to DTX.Ctrl, † $p < 0.05$.

the immune system, may synergize with the local effects on the tumor to achieve optimal outcomes.

In summary, we delineate an ROR-I κ B α /NF- κ B mechanistic pathway that underlies the anti-cancer effects of NOB, alone or in

combination, against TNBC. Our data suggest a possible crosstalk between anti-inflammatory and anti-cancer function of this versatile PMF. These results highlight NOB-ROR as a novel therapeutic strategy against TNBC and inflammation.

DATA AVAILABILITY

All raw data or information related to the current work are available from the corresponding authors upon reasonable request.

REFERENCES

- Bianchini G, Balko JM, Mayer IA, Sanders ME, Gianni L. Triple-negative breast cancer: challenges and opportunities of a heterogeneous disease. *Nat Rev Clin Oncol.* 2016;13:674–90.
- Xu H, Eirew P, Mullaly SC, Aparicio S. The omics of triple-negative breast cancers. *Clin Chem.* 2014;60:122–33.
- Engebraaten O, Vollan HKM, Borresen-Dale AL. Triple-negative breast cancer and the need for new therapeutic targets. *Am J Pathol.* 2013;183:1064–74.
- Zeichner SB, Terawaki H, Gogineni K. A review of systemic treatment in metastatic triple-negative breast cancer. *Breast Cancer.* 2016;10:25–36.
- Fleisher B, Clarke C, Ait-Oudhia S. Current advances in biomarkers for targeted therapy in triple-negative breast cancer. *Breast Cancer.* 2016;8:183–97.
- Walle T. Methoxylated flavones, a superior cancer chemopreventive flavonoid subclass? *Semin Cancer Biol.* 2007;17:354–62.
- Evans M, Sharma P, Guthrie N. Bioavailability of citrus polymethoxylated flavones and their biological role in metabolic syndrome and hyperlipidemia. *InTech;* 2012: 1–19.
- Mulvihill EE, Burke AC, Huff MW. Citrus flavonoids as regulators of lipoprotein metabolism and atherosclerosis. *Annu Rev Nutr.* 2016;36:275–99.
- Huang H, Li L, Shi W, Liu H, Yang J, Yuan X, et al. The multifunctional effects of Nobiletin and its metabolites in vivo and in vitro. *Evid Based Complement Altern Med.* 2016;2016:2918796.
- Ashrafzadeh M, Zarrabi A, Saberifar S, Hashemi F, Hushmandi K, Hashemi F, et al. Nobiletin in cancer therapy: how this plant derived-natural compound targets various oncogene and onco-suppressor pathways. *Biomedicines.* 2020;8:110
- Goh JXH, Tan LT-H, Goh JK, Chan KG, Pusparajah P, Lee L-H, et al. Nobiletin and derivatives: functional compounds from citrus fruit peel for colon cancer chemoprevention. *Cancers.* 2019;11:867.
- Chen C, Ono M, Takeshima M, Nakano S. Antiproliferative and apoptosis-inducing activity of nobiletin against three subtypes of human breast cancer cell lines. *Anticancer Res.* 2014;34:1785–92.
- Ma Y, Ren X, Patel N, Xu X, Wu P, Liu W, et al. Nobiletin, a citrus polymethoxyflavone, enhances the effects of bicalutamide on prostate cancer cells via down regulation of NF- κ B, STAT3, and ERK activation. *RSC Adv.* 2020;10:10254–62.
- Yoshimizu N, Otani Y, Saikawa Y, Kubota T, Yoshida M, Furukawa T, et al. Antitumour effects of nobiletin, a citrus flavonoid, on gastric cancer include: antiproliferative effects, induction of apoptosis and cell cycle deregulation. *Aliment Pharmacol Ther.* 2004;20:95–101.
- Sato T, Koike L, Miyata Y, Hirata M, Mimaki Y, Sashida Y, et al. Inhibition of activator protein-1 binding activity and phosphatidylinositol 3-kinase pathway by nobiletin, a polymethoxy flavonoid, results in augmentation of tissue inhibitor of metalloproteinases-1 production and suppression of production of matrix metalloproteinases-1 and -9 in human fibrosarcoma HT-1080 cells. *Cancer Res.* 2002;62:1025–9.
- Ma W, Feng S, Yao X, Yuan Z, Liu L, Xie Y. Nobiletin enhances the efficacy of chemotherapeutic agents in ABCB1 overexpression cancer cells. *Sci Rep.* 2015;5:18789.
- Baek SH, Kim S-M, Nam D, Lee J-H, Ahn KS, Choi S-H, et al. Antimetastatic effect of nobiletin through the down-regulation of CXC chemokine receptor type 4 and matrix metalloproteinase-9. *Pharm Biol.* 2012;50:1210–8.
- He B, Nohara K, Park N, Park Y-S, Guillory B, Zhao Z, et al. The small molecule nobiletin targets the molecular oscillator to enhance circadian rhythms and protect against metabolic syndrome. *Cell Metab.* 2016;23:610–21.
- Nohara K, Mallampalli V, Nemkov T, Wirianto M, Yang J, Ye Y, et al. Nobiletin fortifies mitochondrial respiration in skeletal muscle to promote healthy aging against metabolic challenge. *Nat Commun.* 2019;10:3923.
- Shinozaki A, Misawa K, Ikeda Y, Haraguchi A, Kamagata M, Tahara Y, et al. Potent effects of flavonoid nobiletin on amplitude, period, and phase of the circadian clock rhythm in PER2::LUCIFERASE mouse embryonic fibroblasts. *PLoS ONE.* 2017;12:e0170904.
- Petrenko V, Gandasi NR, Sage D, Tengholm A, Barg S, Dibner C. In pancreatic islets from type 2 diabetes patients, the dampened circadian oscillators lead to reduced insulin and glucagon exocytosis. *Proc Natl Acad Sci USA.* 2020;117:2484–95.
- Littleton ES, Childress ML, Gosting ML, Jackson AN, Kojima S. Genome-wide correlation analysis to identify amplitude regulators of circadian transcriptome output. *Sci Rep.* 2020;10:21839.
- Mileykovskaya E, Yoo SH, Dowhan W, Chen Z. Nobiletin: targeting the circadian network to promote bioenergetics and healthy aging. *Biochem Biokhim.* 2020;85:1554–9.
- Nohara K, Nemkov T, D'Alessandro A, Yoo SH, Chen Z, et al. Coordinate Regulation of cholesterol and bile acid metabolism by the clock modifier Nobiletin in metabolically challenged old mice. *Int J Mol Sci.* 2019;20:4281
- Takahashi JS. Transcriptional architecture of the mammalian circadian clock. *Nat Rev Genet.* 2017;18:164–79.
- Jetten AM, Kang HS, Takeda Y. Retinoic acid-related orphan receptors alpha and gamma: key regulators of lipid/glucose metabolism, inflammation, and insulin sensitivity. *Front Endocrinol.* 2013;4:1.
- Kojetin DJ, Burris TP. REV-ERB and ROR nuclear receptors as drug targets. *Nat Rev Drug Discov.* 2014;13:197–216.
- Lau P, Fitzsimmons RL, Raichur S, Wang SC, Lechtken A, Muscat GE. The orphan nuclear receptor, RORalpha, regulates gene expression that controls lipid metabolism: staggerer (SG/SG) mice are resistant to diet-induced obesity. *J Biol Chem.* 2008;283:18411–21.
- Sulli G, Lam MTY, Panda S. Interplay between circadian clock and cancer: new frontiers for cancer treatment. *Trends Cancer.* 2019;5:475–94.
- Fu L, Lee CC. The circadian clock: pacemaker and tumour suppressor. *Nat Rev Cancer.* 2003;3:350–61.
- Battaglin F, Chan P, Pan Y, Soni S, Qu M, Spiller ER, et al. Clocking cancer: the circadian clock as a target in cancer therapy. *Oncogene* 2021.
- Fekry B, Ribas-Latre A, Baumgartner C, Deans JR, Kwok C, Patel P, et al. Incompatibility of the circadian protein BMAL1 and HNF4alpha in hepatocellular carcinoma. *Nat Commun.* 2018;9:4349.
- Puram RV, Kowalczyk MS, de Boer CG, Schneider RK, Miller PG, McConkey M, et al. Core circadian clock genes regulate leukemia stem cells in AML. *Cell.* 2016;165:303–16.
- Papagiannakopoulos T, Bauer MR, Davidson SM, Heimann M, Subbaraj L, Bhutkar A, et al. Circadian rhythm disruption promotes lung tumorigenesis. *Cell Metab.* 2016;24:324–31.
- Ye Y, Xiang Y, Ozguc FM, Kim Y, Liu CJ, Park PK, et al. The genomic landscape and pharmacogenomic interactions of clock genes in cancer chronotherapy. *Cell Syst.* 2018;6:314–28 e312.
- Moreno-Smith M, Milazzo G, Tao L, Fekry B, Zhu B, Mohammad MA, et al. Restoration of the molecular clock is tumor suppressive in neuroblastoma. *Nat Commun.* 2021;12:4006.
- Mocellin S, Tropea S, Benna C, Rossi CR. Circadian pathway genetic variation and cancer risk: evidence from genome-wide association studies. *BMC Med.* 2018;16:20.
- Kim H, Lee JM, Lee G, Bhin J, Oh SK, Kim K, et al. DNA damage-induced RORalpha is crucial for p53 stabilization and increased apoptosis. *Mol Cell.* 2011;44:797–810.
- Oh TG, Wang S-CM, Acharya BR, Goode JM, Graham JD, Clarke CL, et al. The nuclear receptor, ROR γ , regulates pathways necessary for breast cancer metastasis. *EBioMedicine.* 2016;6:59–72.
- Nohara K, Kim E, Wirianto M, Mileykovskaya E, Dowhan W, Chen Z, et al. Cardiolipin synthesis in skeletal muscle is rhythmic and modifiable by age and diet. *Oxid Med Cell Longev.* 2020;2020:5304768.
- Reece-Hoyes JS, Walhout AJM, et al. Gateway recombinational cloning. *Cold Spring Harb Protoc.* 2018;2018:pdb.top094912.
- Liu AC, Tran HG, Zhang EE, Priest AA, Welsh DK, Kay SA. Redundant function of REV-ERBalpha and beta and non-essential role for Bmal1 cycling in transcriptional regulation of intracellular circadian rhythms. *PLoS Genet.* 2008;4:e1000023.
- Liu AC, Welsh DK, Ko CH, Tran HG, Zhang EE, Priest AA, et al. Intercellular coupling confers robustness against mutations in the SCN circadian clock network. *Cell.* 2007;129:605–16.
- Yoo SH, Yamazaki S, Lowrey PL, Shimomura K, Ko CH, Buhr ED, et al. PERIOD2::LUCIFERASE real-time reporting of circadian dynamics reveals persistent circadian oscillations in mouse peripheral tissues. *Proc Natl Acad Sci USA.* 2004;101:5339–46.
- Wirianto M, Yang J, Kim E, Gao S, Paudel KR, Choi JM, et al. The GSK-3beta-FBXL21 axis contributes to circadian TCAP degradation and skeletal muscle function. *Cell Rep.* 2020;32:108140.
- Kim HK, Lee SY, Koike N, Kim E, Wirianto M, Burish MJ, et al. Circadian regulation of chemotherapy-induced peripheral neuropathic pain and the underlying transcriptomic landscape. *Sci Rep.* 2020;10:13844.
- Ritchie ME, Phipson B, Wu D, Hu Y, Law CW, Shi W, et al. limma powers differential expression analyses for RNA-sequencing and microarray studies. *Nucleic Acids Res.* 2015;43:e47.
- Jiao X, Sherman BT, Huang da W, Stephens R, Baseler MW, Lane HC, et al. DAVID-WS: a stateful web service to facilitate gene/protein list analysis. *Bioinformatics.* 2012;28:1805–6.
- Yu G, Wang LG, Han Y, He QY. clusterProfiler: an R package for comparing biological themes among gene clusters. *OMICS.* 2012;16:284–7.
- Wang Y, Kumar N, Nuhant P, Cameron MD, Istrate MA, Roush WR, et al. Identification of SR1078, a synthetic agonist for the orphan nuclear receptors RORalpha and RORgamma. *ACS Chem Biol.* 2010;5:1029–34.

51. Anafi RC, Francey LJ, Hogenesch JB, Kim J. CYCLOPS reveals human transcriptional rhythms in health and disease. *Proc Natl Acad Sci USA*. 2017;114:5312–7.
52. Altman BJ, Hsieh AL, Sengupta A, Krishnanaiah SY, Stine ZE, Walton ZE, et al. MYC disrupts the circadian clock and metabolism in cancer cells. *Cell Metab*. 2015;22:1009–19.
53. Lellupitiyage Don SS, Robertson KL, Lin HH, Labriola C, Harrington ME, Taylor SR, et al. Nobiletin affects circadian rhythms and oncogenic characteristics in a cell-dependent manner. *PLoS ONE*. 2020;15:e0236315.
54. Taheri M, Omrani MD, Noroozi R, Ghafouri-Fard S, Sayad A. Retinoic acid-related orphan receptor alpha (RORA) variants and risk of breast cancer. *Breast Dis*. 2017;37:21–25.
55. Xiong G, Wang C, Evers BM, Zhou BP, Xu R. ROR α suppresses breast tumor invasion by inducing SEMA3F expression. *Cancer Res*. 2012;72:1728–39.
56. Du J, Xu R. ROR α , a potential tumor suppressor and therapeutic target of breast cancer. *Int J Mol Sci*. 2012;13:15755–66.
57. Muscat GE, Eriksson NA, Byth K, Loi S, Graham D, Jindal S, et al. Research resource: nuclear receptors as transcriptome: discriminant and prognostic value in breast cancer. *Mol Endocrinol*. 2013;27:350–65.
58. Oh TG, Bailey P, Dray E, Smith AG, Goode J, Eriksson N, et al. PRMT2 and ROR γ expression are associated with breast cancer survival outcomes. *Mol Endocrinol*. 2014;28:1166–85.
59. Delerive P, Monte D, Dubois G, Trottein F, Fruchart-Najib J, Mariani J, et al. The orphan nuclear receptor ROR alpha is a negative regulator of the inflammatory response. *EMBO Rep*. 2001;2:42–48.
60. Hanahan D, Weinberg RA. Hallmarks of cancer: the next generation. *Cell*. 2011;144:646–74.
61. Todoric J, Antonucci L, Karin M. Targeting inflammation in cancer prevention and therapy. *Cancer Prev Res*. 2016;9:895–905.
62. Kropp KN, Schaufele TJ, Fatho M, Volkmar M, Conradi R, Theobald M, et al. A bicistronic vector backbone for rapid seamless cloning and chimerization of alphabeta T-cell receptor sequences. *PLoS ONE*. 2020;15:e0238875.
63. Moser SC, Voerman JSA, Buckley DL, Winter GE, Schliehe C. Acute pharmacologic degradation of a stable antigen enhances its direct presentation on MHC class I molecules. *Front Immunol*. 2017;8:1920.
64. Cai D, Wang J, Gao B, Li J, Wu F, Zou JX, et al. ROR γ is a targetable master regulator of cholesterol biosynthesis in a cancer subtype. *Nat Commun*. 2019;10:4621.
65. Liubomirski Y, Lerrer S, Meshel T, Rubinstein-Achiasaf L, Morein D, Wiemann S, et al. Tumor-stroma-inflammation networks promote pro-metastatic chemokines and aggressiveness characteristics in triple-negative breast cancer. *Front Immunol*. 2019;10:757.
66. Sivick KE, Desbien AL, Glickman LH, Reiner GL, Corrales L, Surh NH, et al. Magnitude of therapeutic STING activation determines CD8(+) T cell-mediated anti-tumor immunity. *Cell Rep*. 2018;25:3074–85 e3075.
67. Wei D, Zhang G, Zhu Z, Zheng Y, Yan F, Pan C, et al. Nobiletin inhibits cell viability via the SRC/AKT/STAT3/Y1AP1 pathway in human renal carcinoma cells. *Front Pharmacol*. 2019;10:690.
68. Ueda HR, Hayashi S, Chen W, Sano M, Machida M, Shigeyoshi Y, et al. System-level identification of transcriptional circuits underlying mammalian circadian clocks. *Nat Genet*. 2005;37:187–92.
69. O'Shea JM, Perkins ND. Regulation of the RelA (p65) transactivation domain. *Biochem Soc Trans*. 2008;36:603–8.
70. Montagut C, Tusquets I, Ferrer B, Corominas JM, Bellosillo B, Campas C, et al. Activation of nuclear factor-kappa B is linked to resistance to neoadjuvant chemotherapy in breast cancer patients. *Endocr Relat Cancer*. 2006;13:607–16.
71. Wang L, Kang F, Li J, Zhang J, Shan B. Overexpression of p65 attenuates celecoxib-induced cell death in MDA-MB-231 human breast cancer cell line. *Cancer Cell Int*. 2013;13:14.
72. Xia Y, Shen S, Verma IM. NF-kappaB, an active player in human cancers. *Cancer Immunol Res*. 2014;2:823–30.
73. Jiang Y, Zhou J, Zhao J, Hou D, Zhang H, Li L, et al. MiR-18a-downregulated RORA inhibits the proliferation and tumorigenesis of glioma using the TNF-alpha-mediated NF-kappaB signaling pathway. *EBioMedicine*. 2020;52:102651.
74. Seitz S, Rick FG, Schally AV, Treszl A, Hohla F, Szalontay L, et al. Combination of GHRH antagonists and docetaxel shows experimental effectiveness for the treatment of triple-negative breast cancers. *Oncol Rep*. 2013;30:413–8.
75. Hong HK, Maury E, Ramsey KM, Perelis M, Marcheva B, Omura C, et al. Requirement for NF-kappaB in maintenance of molecular and behavioral circadian rhythms in mice. *Genes Dev*. 2018;32:1367–79.
76. Spengler ML, Kuropatwinski KK, Comas M, Gasparian AV, Fedtsova N, Gleiberman AS, et al. Core circadian protein CLOCK is a positive regulator of NF-kappaB-mediated transcription. *Proc Natl Acad Sci USA*. 2012;109:E2457–2465.
77. Narasimamurthy R, Hatori M, Nayak SK, Liu F, Panda S, Verma IM. Circadian clock protein cryptochrome regulates the expression of proinflammatory cytokines. *Proc Natl Acad Sci USA*. 2012;109:12662–7.
78. Shen Y, Endale M, Wang W, Morris AR, Francey LJ, Harold RL, et al. NF-kappaB modifies the mammalian circadian clock through interaction with the core clock protein BMAL1. *PLoS Genet*. 2021;17:e1009933.
79. Nohara K, Shin Y, Park N, Jeong K, He B, Koike N, et al. Ammonia-lowering activities and carbamoyl phosphate synthetase 1 (Cps1) induction mechanism of a natural flavonoid. *Nutr Metab (Lond)*. 2015;12:23.
80. Gutierrez-Monreal MA, Trevino V, Moreno-Cuevas JE, Scott SP. Identification of circadian-related gene expression profiles in entrained breast cancer cell lines. *Chronobiol Int*. 2016;33:392–405.

ACKNOWLEDGEMENTS

We thank Dr. Andrew Liu for the generous gifts of circadian reporter plasmids, Dr. Mike Lewis for insightful advice, Drs. Juyeon Jo and Chorong Han for experimental assistance, and Sun Young Kim for transcriptome analysis.

AUTHOR CONTRIBUTIONS

S-HY and ZC designed the project; S-HY, JYY, and ZC supervised research; EK, Y-JK, ZJ, JMK, MW, KRP, JAS, and KO conducted research; all authors contributed to experimental design and data analysis; ZC, S-HY, JYY, and EK prepared the manuscript draft; all authors provided information and/or critical comments during manuscript preparation.

FUNDING

This work is in part supported by The Welch Foundation (AU-1971-20180324) and NIH/NIGMS (R01GM114424) to S-HY, Research Scholar Grants from American Cancer Society (RSG-19-185-01-MPC) to JYY, The Welch Foundation (AU-1731-20190330) and NIH/NIA (R56AG063746, R01AG065984) to ZC.

COMPETING INTERESTS

The authors declare no competing interests.

ADDITIONAL INFORMATION

Supplementary information The online version contains supplementary material available at <https://doi.org/10.1038/s41419-022-04826-5>.

Correspondence and requests for materials should be addressed to Seung-Hee Yoo or Zheng Chen.

Reprints and permission information is available at <http://www.nature.com/reprints>

Publisher's note Springer Nature remains neutral with regard to jurisdictional claims in published maps and institutional affiliations.



Open Access This article is licensed under a Creative Commons Attribution 4.0 International License, which permits use, sharing, adaptation, distribution and reproduction in any medium or format, as long as you give appropriate credit to the original author(s) and the source, provide a link to the Creative Commons license, and indicate if changes were made. The images or other third party material in this article are included in the article's Creative Commons license, unless indicated otherwise in a credit line to the material. If material is not included in the article's Creative Commons license and your intended use is not permitted by statutory regulation or exceeds the permitted use, you will need to obtain permission directly from the copyright holder. To view a copy of this license, visit <http://creativecommons.org/licenses/by/4.0/>.

© The Author(s) 2022, corrected publication 2022